Dossi M., Forte E. and Pipan M.; 2015: *Auto-picking and phase assessment by means of attribute analysis applied to GPR pavement inspection*, proceedings of 8th international workshop on advanced Ground Penetrating Radar, IWAGPR 2015, 7-10 July 2015, Florence, Italy.

Grasmueck M., Weger R.J. and Horstmeyer H.; 2005: *Full-resolution GPR imaging*. Geophysics, 70 (1), K12-K19.

Forte E., Pipan M., Casabianca D., Di Cuia R. and Riva A.; 2012: *Imaging and characterization of a carbonate hydrocarbon reservoir analogue using GPR attributes*. Journal of Applied Geophysics, Special Issue: Recent, Relevant and advanced GPR studies in Applied Geophysics, 81, 76-87.

Young R.A., Deng Z., Marfurt K.J. and Nissen S.E.; 1997: 3-D *dip filtering and coherence applied to GPR data: a study*. The Leading Edge, 16, 1011–1018.

McClymont, A.F. *et al*.; 2008: *Visualization of active faults using geometric attributes of 3D GPR data: an example from the Alpine Fault Zone, New Zealand*. Geophysics, 73(2), B11–B23.

Zhao W., Forte E., Pipan M. and Tian G.; 2013: *Ground penetrating radar (GPR) attribute analysis for archeological prospection*. Geophysics, 97, 107-117.

Zhao W., Forte E. and Pipan M.; 2016a: *Texture Attribute Analysis of GPR Data for Archaeological Prospection*. Pure and Applied Geophysics, 173, 2737–2751.

Zhao W., Forte E., Colucci R.R. and Pipan M.; 2016b: *High-resolution glacier imaging and characterization by means of GPR attribute analysis*. Geophys. J. Int., 206(2), 1366–1374.

Zhao W., Forte E., Fontolan G. and Pipan M.; 2018: *Advanced GPR imaging of sedimentary features: integrated attribute analysis applied to sand dunes*. Geophysical Journal International, 213, 1, 147–156.

## HAMILTONIAN MONTE CARLO INVERSION OF SURFACE WAVE DISPERSION CURVES: PRELIMINARY RESULTS

**A. Salusti[1], M. Aleardi[2]**

*[1] University of Florence, Earth Sciences Dept., Florence, Italy*

*[2] University of Pisa, Earth Sciences Dept., Pisa, Italy*

**Introduction.** Rayleigh wave measurements are highly sensitive to the S-wave velocity (*Vs*) and for this reason they are attractive for geotechnical characterization or seismic site response studies (Socco and Strobbia 2004). Over the last years, the full-waveform inversion of surface waves is getting growing attention thanks to the increased computational power of modern parallel architectures (Gross *et al*. 2017). Well-established methods rely on dispersion curve inversion under the assumption of a 1D subsurface structure. The dispersion curve inversion is a highly non-linear and ill-conditioned problem. For these reasons, it is crucial adopting inversion approaches that efficiently converge toward the global minimum.

In this context, local inversion methods exhibit fast convergence rates but limited capability to explore the model parameter space, resulting in a final solution highly dependent on the initial model. Global search algorithms (genetic algorithms, simulated annealing) exhaustively explore the model space but they usually require a considerable computational effort ( Cercato, 2011). Markov Chain Monte Carlo (MCMC) algorithms exhibit global convergence capabilities and honour the importance sampling principle, but they usually rely on specific MCMC recipes in order to maintain the computational cost affordable. More specifically, MCMC methods are primarily affected by low acceptance rates and show strong correlations between the sampled models. Hamiltonian Monte Carlo (MC) algorithm was designed to circumvent these two critical issues of MCMC algorithms. HMC treats a model as the mechanical analogue of a particle that moves from its current position (current model) to a new position (proposed model) along a given trajectory. The geometry of the trajectory is controlled by the misfit function, which is interpreted as potential energy ($U$), and by the kinetic energy ($K$) and the mass of the particle. After the so-called burn-in period, the ensemble of HMC sampled models can be used to numerically derive the so-called posterior probability density (PPD) function in the model

space. In this work we apply an HMC algorithm for inverting Rayleigh waves dispersion curves on synthetic and experimental tests. We inverted for *Vs*, *Vp*/*Vs* ratio and layer thicknesses, whereas the density is kept fixed during the inversion at a constant value. The implemented HMC algorithm requires the number of layers be defined as input to the inversion. However, the limited computational cost of the HMC inversion allows us to perform different inversions with different model space parameterizations. Then, standard statistical tools (such as $\chi^2$ probability or the Bayesian information criterion "BIC") can be used to define the most appropriate model parameterization to use.

**Method.** The HMC relies on the Bayesian inversion framework. In this context the solution of an inverse problem is the posterior probability density (PPD) function that is defined as follows:

$$p(\mathbf{q}\,|\,\mathbf{d}) = \frac{p(\mathbf{d}\,|\,\mathbf{q})p(\mathbf{q})}{p(\mathbf{d})} \tag{1}$$

where $\mathbf{d}$ is $N$-dimensional observed data vector, and $\mathbf{q}$ is the $Q$-dimensional model parameter vector. The left-hand side term of equation (1) represents the target PPD that could be numerically estimated from the ensemble of models sampled during the Monte Carlo sampling. HMC algorithm treats a model as the mechanical analogue of a particle that moves from its current position (current model) to a new position (proposed model) along a trajectory. This trajectory is determined by the potential energy ($U$), the kinetic energy ($K$) and the mass matrix ($\mathbf{M}$). The potential energy is the negative natural logarithm of the posterior (see equation 1) or in other terms is the misfit function associated to the inverse problem. In this context more plausible models with large values of the posterior are associated to low potential energies. HMC determines the kinetic energy by introducing an auxiliary variable (momentum variable) $\mathbf{p}$ that is defined over a Q-dimensional space:

$$K(\mathbf{p}) = \frac{1}{2}\,\mathbf{p}^T\,\mathbf{M}^{-1}\mathbf{p}, \tag{2}$$

where $\mathbf{M}$ is the $Q\times Q$ mass matrix that must be accurately set to ensure the convergence of the HMC algorithm (see Fictner *et al*. 2019). The vectors $\mathbf{p}$ and $\mathbf{q}$ define the so-called phase space. After defining the kinetic and potential energies, the model $\mathbf{q}$ moves through the 2×Q-phase space according to Hamilton's equations:

$$\frac{d\mathbf{q}_i}{dt} = \frac{\partial K}{d\mathbf{p}_i}, \qquad \frac{d\mathbf{p}_i}{dt} = -\frac{\partial U}{d\mathbf{q}_i}, \quad \text{with } i = 1, 2,\ldots, Q\,. \tag{3}$$

where $t$ indicates the artificially introduced time variable. For each current model $\mathbf{q}$, and for each iteration, HMC executes the following steps:

1. Randomly draw the Q momenta $\mathbf{p}_i$ from the normal distribution $\left(-\frac{1}{2}\,\mathbf{p}^T\,\mathbf{M}^{-1}\mathbf{p}\right)$;
2. Derive the proposed model $\mathbf{q}(t)$ and the new momenta $\mathbf{p}(t)$ by solving Hamilton's equations (3) for a given propagation time $t$. In this work we use the leap-frog method to solve this equation (Betancourt, 2017). The propagation time $t$, together with the mass matrix plays a crucial influence on the convergence of the sampling;
3. Accept the proposed model with probability $\alpha$:

$$\alpha = \min\left[1, \frac{\exp[-H(\mathbf{p}(t), \mathbf{q}(t))]}{\exp[-H(\mathbf{p}, \mathbf{q})}\right], \tag{4}$$

where the total energy or Hamiltonian of the model is the sum of kinetic and potential energies ($H = U + K$). If accepted, the proposed $\mathbf{q}(t)$ point constitutes the starting models for the next trajectory ($\mathbf{q} = \mathbf{q}(t)$). Otherwise, the current model $\mathbf{q}$ is again used as the

starting point in the following iteration;

4. Return to step 1.

In this work the potential energy is defined as:

$$U(\mathbf{q}) = \frac{1}{2}\Big(\mathbf{d} - G(\mathbf{q})\Big)^T \mathbf{C}_d^{-1}\Big(\mathbf{d} - G(\mathbf{q})\Big) + \frac{1}{2}\Big(\mathbf{q} - \mathbf{q}_{prior}\Big)^T \mathbf{C}_q^{-1}\Big(\mathbf{q} - \mathbf{q}_{prior}\Big), \quad (5)$$

where $G$ is the non-linear forward modelling operator that computes the dispersion curves for the considered model, $\mathbf{C}_d$ is the data covariance matrix, $\mathbf{d}$ is the observed dispersion curve, $\mathbf{q}_{prior}$ is the prior model with prior covariance matrix given by $\mathbf{C}_q$. In this work, the mass matrix is computed as a local approximation (around the considered model) of the posterior covariance matrix (see Fictner *et al*. 2019):

$$\mathbf{M} = \Big(\mathbf{J}^T \mathbf{C}_d^{-1}\mathbf{J} + \mathbf{C}_q^{-1}\Big), \quad (6)$$

where $\mathbf{J}$ is the Jacobian matrix that expresses the partial derivative of the data with respect to model parameters. We assume Gaussian distributed and uncorrelated a-priori model parameters. We employ very simple Gaussian prior models: the prior for *Vs* has a mean value of 160 m/s with a standard deviation of 30 m/s, whereas the prior for layer thickness has a mean value of 5 with a standard deviation of 2. Obviously, different prior models can be easily included into the inversion framework. For example, we can consider a depth-dependent prior model for *Vs* or even non-Gaussian priors. The starting point for the HMC sampling is randomly generated from the prior.

**Synthetic and experimental inversion tests.** We start by considering a very simple and schematic synthetic model constituted by two layers separated by an interface located at 8 m depth. In this example our aim is to compare the uncertainties affecting the estimated model when the dispersion curves lie in different frequency bands. In the first case the dispersion curve extends over [4-30 Hz], whereas in the second case the dispersion curve lies in the interval [6-30 Hz]. In the performed inversions the dispersion curves have been analytically computed from

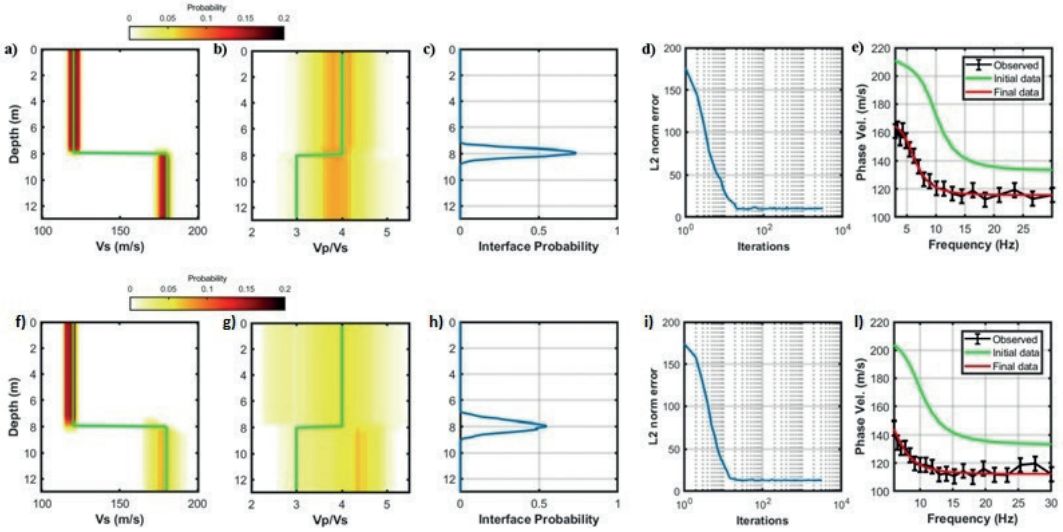


Fig. 1 - Synthetic inversion results for a 2-layer model. From a) to e): inverted bandwidth between 4 and 30 Hz. From f) to l): inverted bandwidth between 6 and 30 Hz. In both panels we represent from left to right: True model (green line) and marginal *Vs* PPD (colour scale); True Vp/Vs model (green line) and marginal Vp/Vs PPD (colour scale); Marginal PPD for interface location; Evolution of the L2 norm misfit; comparison between the observed noisy data (black line), the data generated on the starting model (red line) and the data generated on the last sampled model (green line).

the reference model and contaminated with Gaussian random noise with a standard deviation of 5.

We start by considering the schematic 2-layer model. In this case our aim is to compare the uncertainties affecting the final solution when the dispersion curves lie in different frequency bands. In the first test the dispersion curve extends over [3-30 Hz], whereas in the second case the dispersion curve lies in the interval [6-30 Hz]. Both examples consider a correct number of layers equal to 2. In Fig. 1 top 5 images we represent the results for the 3-30 Hz example. The marginal PPDs of *Vs* and interface location show that the inversion perfectly recovers the true model and that the estimated layer depth position is perfectly located at 8 meters. Differently the *Vp*/*Vs* ratio is not recovered, and the posterior distribution is still very similar to the prior with a depth-independent MAP value equal to 4. Note the fast convergence rate of the chain that need about 30 iterations to reach the stationary regime. The comparison between the observed dispersion curve and the dispersion curves computed on the starting model and on the model sampled at the last iteration, demonstrates that the algorithm perfectly predicts the observed data. Figure 1, bottom 5 images, shows the results for the 6-30 Hz example. We observe that the *Vs* of the first layer has been recovered with the same accuracy of the previous example. Differently, the position of the interface and particularly the velocity of the deepest layer are now estimated with higher uncertainties. This is mainly related to the fact that the low frequencies are crucial to constraint the *Vs* of the deepest layer. Indeed, this model parameter influences the

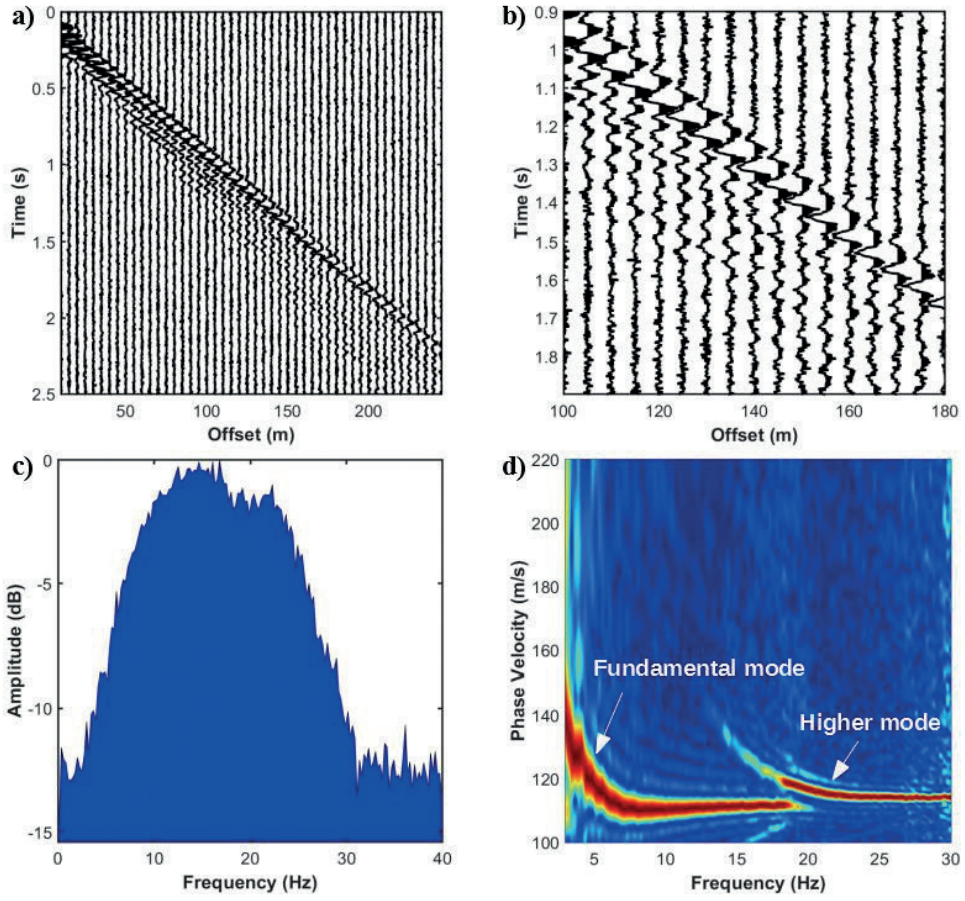


Fig 2 - a) Synthetic and noise-contaminated shot gather. b) Close-up of a). c) Fourier amplitude spectra of a). d) Phase velocity spectra derived on a): blue and red colors are low and high amplitude values, respectively.

slope of the fundamental mode at low frequencies (Socco and Strobbia, 2004). The *Vp*/*Vs* ratio is not recovered with a posterior distribution similar to the prior. The computed $\chi^2$ probability ($p(\chi^2)$) and the BIC values obtained for a correct 2-layer parametrization are $p(\chi^2)$=0.0408 and BIC=34.61, we also performed an inversion with an erroneous 3-layer parameterization (not shown here for brevity) that provides a $p(\chi^2)$ and BIC values of 0.0105 and 44.54, respectively. The higher $p(\chi^2)$ and lower BIC values clearly indicate that the 2-layer is the most appropriate parameterization, thus proving that these statistical tools could constitute a valid help to select the optimal model parameterization.

We now describe the results provided for the experimental inversion tests. In this case the observed dispersion curves have been picked on the frequency-phase velocity spectra derived from synthetic shot gathers computed making use of the reflectivity method. We employ a 15 [Hz] Ricker wavelet as the source signature with a sampling interval of 2 [ms]. We simulate an off-end acquisition geometry with a minimum offset of 10 m and 48 receivers equally spaced of 5 m, resulting in a maximum offset of 245 m.

Fig. 2 shows a synthetic shot gather, the Fourier amplitude spectra of the signal and its phase velocity spectra.

Note that the *Vs* of the second layer is lower than that of the first layer: this velocity inversion complicates the picking of the fundamental mode because higher modes become more energetic than the fundamental mode at high frequencies. In cases of velocity inversions the consideration of only the fundamental model severely increases the ill-conditioning of the inversion procedure, and for this reason in these situations higher modes are often of crucial importance to better constraint the final estimates.

Fig. 3 displays the inversion results. The *Vs* of the shallowest layer is perfectly resolved and also the *Vs* of the second layer is well predicted, although the MAP solution slightly

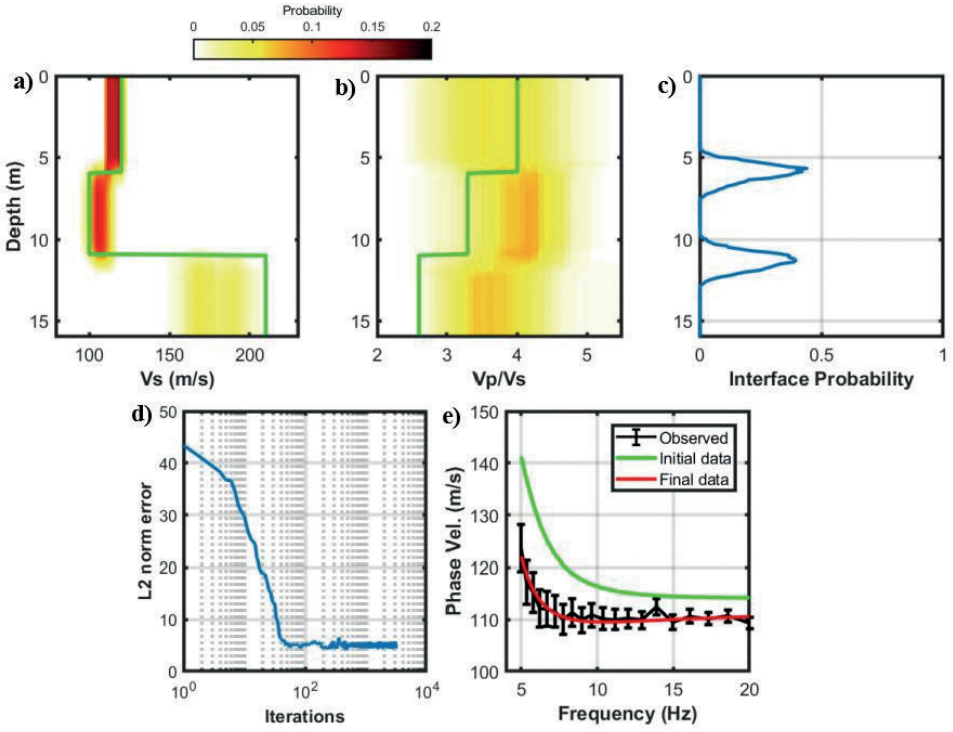


Fig. 3 - a) True Vs model and marginal Vs PPD (colour scale). b) True Vp/Vs model and marginal Vp/Vs PPD (colour scale). c) Marginal PPD for interface location. d) Evolution of the L2 norm misfit. e) Comparison between the picked dispersion curve, data generated on the starting model and the data generated on the last sampled model.

overestimates the true velocity value. Notwithstanding the velocity inversion, the algorithm accurately predicts a low velocity layer. The uncertainties in the estimated *Vs* rapidly increase as the depth increases and the velocity of the deepest layer is not well recovered with a MAP solution that significantly underestimates the actual velocity value. The *Vp*/*Vs* ratio is again not resolved. Fig 3.c demonstrates that the HMC algorithm correctly identifies the position of the interfaces. Only 30 iterations are enough to converge toward the stationary regime, whereas the observed data is still perfectly matched.

**Conclusions.** We implemented a Hamiltonian Monte Carlo (HMC) algorithm for Rayleigh wave dispersion curve inversion. This approach ensures reliable assessment of the posterior uncertainties in highly non-linear inverse problems and guarantees efficient sampling even in high-dimensional model spaces. This ability rests on the exploitation of derivative information of the misfit function that is not considered by other standard Monte Carlo methods. In this work, the algorithm has been implemented for a Gaussian prior model, but another outstanding benefit of HMC is the possibility to consider either parametric or not-parametric priors. Our tests demonstrated the applicability of the proposed HMC approach for Rayleigh wave dispersion curve inversion and the possibility to derive the optimal model parameterization by adopting standard statistical tools. In particular, the algorithm yielded uncertainty quantifications and model predictions in accordance with the expected model parameter illuminations. The HMC algorithm presented here can be easily extended to include higher modes. We are now testing the algorithm on field data inversions. Furthermore, we are extending the presented HMC approach to full-waveform inversion of surface waves.

**References**

Betancourt, M. (2017). A conceptual introduction to Hamiltonian Monte Carlo. arXiv preprint arXiv:1701.02434.

Cercato, M. (2011). Global surface wave inversion with model constraints. Geophysical Prospecting, 59(2), 210-226.

Duane, S., Kennedy, A. D., Pendleton, B. J., and Roweth, D. (1987). Hybrid Monte Carlo. Physics Letters B, 195, 216–222.

Socco L.V. and Strobbia C. (2004). Surface-wave method for nearsurface characterization: a tutorial. Near Surface Geophysics 2, 165–185.

## ADVANCED GPR DATA ANALYSIS FOR GLACIOLOGY: A MULTI-YEAR STUDY ON THE MARMOLADA GLACIER (DOLOMITES, ITALY)

**I. Santin[1], E. Forte[1], M. Pavan[2], M. Valt[3], M. Žebre[4], R.R. Colucci[5]**

*[1] Department of Mathematics and Geosciences, University of Trieste, Italy*

*[2] Department of Earth, Environmental and Life Sciences, University of Genova, Italy*

*[3] ARPAV - Agenzia Regionale per la Prevenzione e Protezione Ambientale del Veneto, Arabba, BL, Italy*

*[4] Department of Geography & Earth Sciences, Aberystwyth University, United Kingdom*

*[5] Department of Earth System Sciences and Environmental Technology, CNR – ISMAR, Basovizza, Italy*

**Introduction.** Knowing the evolution of glaciers' changes in shape and size is extremely useful for both glaciological studies (Carturan *et al*., 2013), practical application (Diolaiuti *et al*., 2006) and, even more important, for global climate assessment (Zemp *et al*., 2013). For this reason, long-term glacier monitoring has been performed generally since the beginning of the last century to understand the physical processes which lead to glaciers' response to climate change (Haeberli *et al*., 2013). In order to monitor mass variations of a glacier with time (i.e. its mass balance) and provide more realistic forecasts about its future evolution, detailed information about volume and internal structure is required in addition to classical linear and areal measurements. Ground Penetrating Radar (GPR) has proved to be an efficient instrument